frontiers in Environmental Chemistry

ORIGINAL RESEARCH
published: 14 February 2022
doi: 10.3389/fenvc.2022.784385

Tracking the Lithium and Strontium Isotope Signature of Hydrothermal Plume in the Water Column: A Case Study at the EMSO-Azores Deep-Sea Observatory

Lise Artigue[1]*, *Valérie Chavagnac*[1], *Christine Destrigneville*[1], *Bruno Ferron*[2] and *Cécile Cathalot*[3]

[1]Géosciences Environnement Toulouse, GET, CNRS, UPS, Université de Toulouse, IRD, Toulouse, France, [2]Laboratoire d'Océanographie Physique et Spatiale, Univ Brest-CNRS-IFREMER-IRD-IUEM, Plouzané, France, [3]Laboratoire des Cycles Géochimiques et Ressources, LCG, IFREMER, Plouzané, France

OPEN ACCESS

Edited by:
Nathalie Vigier, UMR7093 Laboratoire d'océanographie de Villefranche (LOV), France

Reviewed by:
Romain Millot, Bureau de Recherches Géologiques et Minières, France
Svetoslava Todorova, Syracuse University, United States

***Correspondence:**
Lise Artigue
lise.artigue@get.omp.eu

Specialty section:
This article was submitted to Inorganic Pollutants, a section of the journal Frontiers in Environmental Chemistry

Received: *27 September 2021*
Accepted: *10 January 2022*
Published: *14 February 2022*

Citation:
Artigue L, Chavagnac V, Destrigneville C, Ferron B and Cathalot C (2022) Tracking the Lithium and Strontium Isotope Signature of Hydrothermal Plume in the Water Column: A Case Study at the EMSO-Azores Deep-Sea Observatory. Front. Environ. Chem. 3:784385. doi: 10.3389/fenvc.2022.784385

Lithium (Li) and strontium (Sr) are two economically relevant chemical elements whose oceanic biogeochemical cycles are not fully constrained. In particular, how they disperse and behave from hydrothermal sources into the water column is understudied while hydrothermal systems on the global mid-ocean ridge network (~67,000 km) represent one of the main sources of Li. This study aims to provide new insights on the dissolved Li (DLi) and Sr (DSr) behavior in the water column. Here, we present for the first time the DLi and DSr elemental and isotopic (δ^7Li, and $^{87}Sr/^{86}Sr$) profiles from six casts distributed over the Lucky Strike hydrothermal vent field (LSHF, Mid-Atlantic Ridge). The DLi and DSr results reflect a hydrothermal contribution to the water column up to ~300 m above the seafloor that can be quantified by up to 10% based on the DLi dataset. For increasing hydrothermal contribution the δ^7Li values of the water column become heavier most likely due to mineral–seawater interactions, i.e., manganese oxide formed during the mixing of hydrothermal fluid and seawater. Contrarily to the DLi, DSr, and δ^7Li datasets, the hydrothermal contribution to the water column is not evidenced by the $^{87}Sr/^{86}Sr$ ratios that fall within the range of oligotrophic oceanic waters. Surprisingly, some geographically distant casts display at the same depth identical DLi and DSr concentrations or similar δ^7Li signatures. We attribute these features to the current dynamics above the LSHF, suggesting that the hydrothermal signature of the western casts can overprint those of the eastern and center casts in less than 1 h at the LSHF km-scale. Overall, this study highlights that 1) as for many elements, DLi, DSr, and δ^7Li can be used to track the hydrothermal signature to the water column at a km-scale whereas $^{87}Sr/^{86}Sr$ cannot, 2) local currents play a major role in advecting the hydrothermal contribution away from the hydrothermal sources, and 3) mineral–seawater interaction processes are at play during the mixing between hydrothermal fluid and seawater and impact the δ^7Li hydrothermal signature. Our study suggests that chemical tracers of hydrothermal input have to be chosen depending on the spatial scale of the studied area.

Keywords: hydrothermal vent, water column, lucky strike, EMSO-Azores observatory, lithium, strontium, isotopes

INTRODUCTION

A better understanding of lithium (Li) and strontium (Sr) oceanic biogeochemical cycles is needed nowadays based on two main issues: 1) their oceanic cycles are still under debate, and 2) they are two economically relevant elements. Li and Sr are widely used to estimate several geochemical processes notably at the water/rock interface (Huh et al., 1998; Brunskill et al., 2003; Davis et al., 2003) such as continental weathering (Pistiner and Henderson, 2003; Vance et al., 2009; Millot et al., 2010) or hydrothermal alteration of oceanic crust (Barker et al., 2008; Araoka et al., 2016; Chavagnac et al., 2018a). It is generally admitted that dissolved riverine inputs and hydrothermal inputs are the two main sources of Li and Sr to the ocean (Albarède et al., 1981; Palmer and Edmond, 1989; Allègre et al., 2010; Tomascak et al., 2016; von Strandmann et al., 2020). Nevertheless, there are still unresolved issues concerning the complex Li and Sr oceanic budget (Stoffynegli and Mackenzie, 1984; Huh et al., 1998; Davis et al., 2003; Vance et al., 2009). The isotopic composition of marine Li is heavier than that of its sources, implying that there are sinks that preferentially remove light Li, i.e., secondary clay formation (Tomascak et al., 2016; von Strandmann et al., 2020). However, uncertainties remain regarding, for example, the impact on the marine Li isotope budget of groundwater discharges (Mayfield et al., 2021), or of clay authigenesis (Andrews et al., 2020). Regarding the marine Sr isotopic budget, it is unbalanced as the flux of unradiogenic hydrothermal Sr is too low by a factor 3 to balance the flux of radiogenic river Sr (Palmer and Edmond, 1989; Bickle and Teagle, 1992; Davis et al., 2003; Teagle et al., 2003). Many studies have worked on closing the marine Sr budget by proposing the contributions of unradiogenic Sr sources such as intensive weathering on volcanic islands, island arcs and oceanic islands (Allègre et al., 2010), submarine groundwater discharge (Allègre et al., 2010; Beck et al., 2013; Trezzi et al., 2017; El Meknassi et al., 2020), and dissolution of river-transported particles (Jones et al., 2012a; Jones et al., 2012b; Jones et al., 2014). Alternatively, other studies suggested that the marine Sr budget reflects variation through time in chemical weathering fluxes due to periodic glaciation (non-steady-state marine Sr budget; Vance et al., 2009; Krabbenhoft et al., 2010; Pearce et al., 2015) or variation in the composition and age structure of continental bedrock (Peucker-Ehrenbrink and Fiske, 2019). A major drawback in our understanding of the Sr and Li oceanic cycles is their behavior in the water column, away from the continental margin. Several studies have notably shown that dissolved metals from hydrothermal origin such as iron and aluminum can be transported over a hundred to thousand kilometers away from their source and can even impact productive layers (Measures et al., 2015; Resing et al., 2015; Guieu et al., 2018). It is questionable whether this type of transport can also affect Li and Sr of hydrothermal origin, particularly Li for which hydrothermalism is one of the most dominant sources to the ocean (Araoka et al., 2016; Tomascak et al., 2016, and reference therein).

Li and Sr are also economically important metals. Li is notably used in Li-ion batteries and Sr in ceramic ferrite magnets. The Li and Sr resources on land are fairly well identified for both elements. The world's Li resources are found at ~59% in brines, ~25% in minerals, and the rest in clays, geothermal waters, and oil field brines (Gruber et al., 2011; Kavanagh et al., 2018). The Sr resources are mainly found in celestite and strontianite deposits (Ehya et al., 2013; Singerling and Ober, 2018). Since 2020, Li and Sr have been considered "critical raw materials" by the European Union, i.e., highly important economically but with a high supply risk (European Commission, 2020, *Study on the EU's List of Critical Raw Materials—Final Report*, 2020). Therefore, several studies investigate the feasibility to extract Li and Sr from seawater (Vikström et al., 2013; Hong et al., 2018; Ryu et al., 2020), and in particular Li from black smokers hydrothermal vents that contain 10–20 times more Li than seawater (European Commission, 2012; Chavagnac et al., 2018a). Yet, the effects of deep-sea mining on the marine environment need to be assessed notably through studies on the hydrothermal role in marine biota and element oceanic biogeochemical cycles.

This study presents Li and Sr elemental and isotopic compositions of six profiles in the water column over the Lucky Strike Hydrothermal Field (LSHF), as well as six current speed intensities and direction profiles. The LSHF field has been continuously monitored and studied since 2010 as part of the EMSO-Azores observatory (Colaço et al., 2011) which allows comparison of our water column results with the previously determined hydrothermal fluid compositions. We provide new insights on hydrothermal DLi and DSr dispersion in the water column. Once combined to their isotopic composition, we constrain processes at play during the mixing between hydrothermal fluid and seawater at the LSHF km-scale.

MATERIALS AND METHODS

Study Area

The Lucky Strike Hydrothermal Field (LSHF) is located ~400 km to the Southwest of the Azores archipelago on the Mid-Atlantic Ridge at 37°17′N and 32°20′W (**Figure 1A**; Langmuir et al., 1997; Von Damm et al., 1998). This 1 km^2 hydrothermal vent field consists of 20–30 active vents distributed around a fossil lava lake (apart from Capelinhos vent) surrounded by three ancient volcanic cones (Fouquet et al., 1995; Langmuir et al., 1997; Von Damm et al., 1998; Charlou et al., 2000; Ondréas et al., 2009; Escartin et al., 2015). **Figure 1B** presents the LSHF bathymetric map [~1550–1750 m below sea level (mbsl)] with 12 active hydrothermal sites spatially located to the North East (Sintra and Y3), the South East (Aisics, Tour Eiffel, and Isabel), the North West (Jason, and Elisabeth), and the South West (Helene, Nuno, Crystal, South Crystal, Sapins, White Castle, and Cypres) of the fossil lava lake.

CTD Data and Sample Collection

During the MoMARsat'19 EMSO-Azores maintenance cruise on-board the *R.V. Pourquoi Pas?* (June–July 2019; Sarradin and Legrand, 2019), seawater samples were collected at six selected CTD casts. The selected casts cover the LSHF situated to the

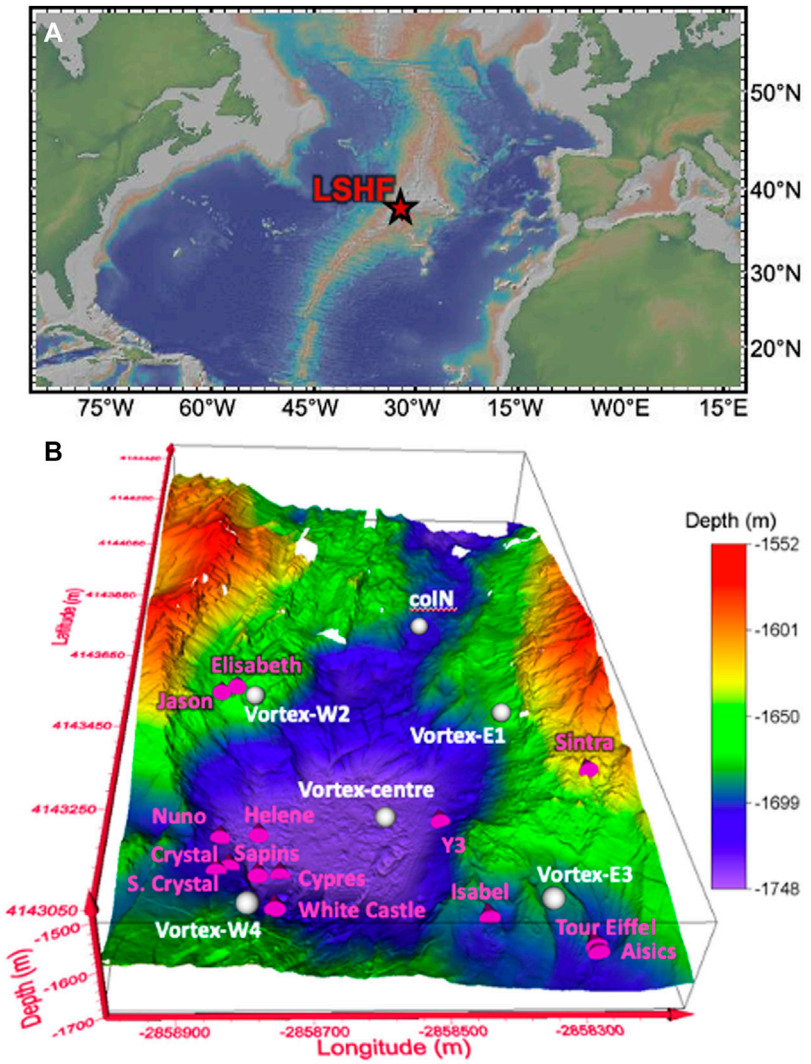

FIGURE 1 | (A) A map of the Lucky Strike Hydrothermal Field (LSHF) location (http://www.geomapapp.org; Ryan et al., 2009), **(B)** A 3D bathymetric map of the LSHF (Ondréas et al., 2009) where active vent and CTD cast locations are reported as pink 3D cones and white spheres, respectively.

North (coIN), West (Vortex-W2 and -W4), East (Vortex-E1 and -E3), and at the center (Vortex-centre) of the fossil lava lake (**Figure 1B**).

Vertical CTD casts used a SeaBird SBE-25 that sampled pressure, temperature, and conductivity at 8 Hz. The mean downcast and upcast CTD velocity was 0.7 m/s. Seawater samples were collected during the upcast between 1722 and 1478 mbsl using a 8 L PVC Ocean Test Equipment (OTE) externally closing bottles and mounted on the CTD carousel. The CTD was stopped for 30 s before firing the bottles to limit the impact of the carousel wake on the samples. Upon recovery, the samples were transferred into a dedicated chemical lab for fluid extraction. The samples were filtered into 250 ml low-density polyethylene bottles (LDPE, Nalgene) washed with diluted hydrochloric acid and rinsed with ultrapure milli-Q water before use. Each subsample was kept in cold storage (~4°C) until its analysis. In total, 30 samples were analyzed for dissolved cations (DCa, DK, DMg, DNa), anions (DCl, DBr, DSO_4), and dissolved Li (DLi) and Sr (DSr) elemental and isotopic compositions.

CTD data were processed with the Seabird data processing software (filtering, temperature-conductivity alignment, thermal mass correction, data editing). The carousel downcast was stopped 15 m above the seafloor. The carousel was equipped with two 300 kHz RDI LADCP data, one up- and one down-looker. Velocity profiles with a 10-m vertical resolution were produced from the combination of the two LADCPs using the LDEO software (version IX.12).

Elemental and Isotopic Analysis

All the chemical analyses were conducted at the Observatoire Midi-Pyrénées.

The analytical methods used for major dissolved cations (DCa, DK, DMg, DNa), and anions (DCl, DBr, DSO_4) analyses on

TABLE 1 | Dissolved lithium and strontium elemental and isotopic compositions at six CTD casts from the Momarsat'19 cruise. The calculated hydrothermal fluid contribution in percentage (fHF, calculated based on DLi concentration) is also displayed for each sample.

Station name	Longitude (W)	Latitude (N)	Depth (m)	DLi ± 1SD (μmol/L)	δ7Li (‰)	DSr ± 1SD (μmol/L)	87Sr/86Sr ± 2SE	fHF (%)
Vortex-centre	–32.279	37.292	1555	17 ± 8	29.4	86 ± 2	0.709182 ± 0.000004	0
			1629	23 ± 2	33.2	89 ± 1	0.709182 ± 0.000004	0
			1679	28 ± 3	28,0	90 ± 1	0.709173 ± 0.000004	1
			1705	29 ± 3	28.7	94 ± 2	0.709181 ± 0.000004	1
			1722	33 ± 3	27.3	90 ± 1	0.709178 ± 0.000004	3
Vortex-W2	–32.282	37.294	1480	51 ± 2	36.1	92 ± 1	0.709175 ± 0.000004	8
			1555	52 ± 2	26.9	98 ± 1	0.709178 ± 0.000005	9
			1604	49 ± 3	29.3	96 ± 1	0.709168 ± 0.000004	8
			1630	54 ± 2	34.2	97 ± 1	0.709172 ± 0.000004	9
			1647	50 ± 2	28.7	94 ± 1	0.709171 ± 0.000004	8
Vortex-E1	–32.276	37.294	1478	35 ± 5	25.9	92 ± 2	0.709170 ± 0.000004	3
			1554	30 ± 3	30.9	87 ± 1	0.709171 ± 0.000004	2
			1605	33 ± 4	30.2	84 ± 1	0.709178 ± 0.000005	3
			1629	39 ± 3	27,0	89 ± 1	0.709166 ± 0.000005	4
			1655	38 ± 4	27.5	87 ± 2	0.709170 ± 0.000005	4
colN	–32.278	37.297	1504	39 ± 4	26.8	92 ± 1	0.709179 ± 0.000004	4
			1580	46 ± 3	27.7	92 ± 1	0.709184 ± 0.000004	7
			1630	39 ± 4	27.9	92 ± 2	0.709182 ± 0.000004	4
			1655	49 ± 2	28.6	93 ± 1	0.709168 ± 0.000005	8
			1680	43 ± 4	26.6	93 ± 2	0.709174 ± 0.000004	6
Vortex-W4	–32.282	37.29	1505	44 ± 3	29.9	95 ± 1	0.709175 ± 0.000004	6
			1580	43 ± 6	28.3	94 ± 3	0.709171 ± 0.000004	6
			1630	36 ± 2	32.3	96 ± 2	0.709175 ± 0.000004	4
			1655	57 ± 3	29.3	95 ± 1	0.709181 ± 0.000004	10
			1680	56 ± 2	29.1	98 ± 2	0.709172 ± 0.000004	10
Vortex-E3	–32.276	37.29	1481	34 ± 3	29.4	91 ± 2	0.709174 ± 0.000006	3
			1555	43 ± 5	28.1	90 ± 1	0.709175 ± 0.000005	6
			1605	40 ± 3	27.6	90 ± 1	0.709168 ± 0.000006	5
			1631	51 ± 4	31.5	89 ± 2	0.709171 ± 0.000005	8
			1657	49 ± 4	30.2	95 ± 1	0.709171 ± 0.000006	8

seawater are detailed in Besson et al. (2014), Chavagnac et al. (2018a), and Leleu (2017) and will be briefly described later. Seawater samples were diluted at 30 fold for cation and anion concentration measurements. Cation concentrations were determined with an inductively coupled plasma atomic emission spectrometer (ICP-AES) Horiba Ultima2 instrument, with an analytical precision better than 2%. Cation concentrations were quantified by the calibration curve method with an IAPSO seawater standard solution (OSIL Ltd., United Kingdom) diluted at 10–100 fold with Milli-Q water. The analytical drift correction was assessed by the standard bracketing method every eight samples. Detection limits were determined by daily repeated measurements of blank solutions (n = 10) at 0.001 mmol/L for DCa, 0.002 mmol/L for both DK and DMg, and 0.1 mmol/L for DNa. Anion concentrations were determined by anionic chromatography (Dionex ICS-2000) equipped with a specific column for a highly charged matrix (DIONEX IC AS19), calibrated with IAPSO seawater standard diluted at 10–50 fold with Milli-Q water, and with an analytical precision better than 2%. The cations and anions concentrations are reported in **Supplementary Table S1** with their respective uncertainties (1SD) calculated by error propagation.

For DLi, and DSr measurements, seawater samples were doped with a prepared DLi and DSr mono-elemental solution. The dissolved Li and DSr concentrations were then measured with ICP-AES and quantified by the method of standard addition with a doped IAPSO standard ranging from 24.6 μmol/L to 386.2 μmol/L for DLi, and 88.0–137.4 μmol/L for DSr. The analytical drift correction, as well as the detection limit (0.2 μmol/L for DLi and 0.002 μmol/L for DSr, n = 10), was assessed as for cations. The dissolved Li and DSr measurements are reported in **Table 1** with their respective uncertainties (1SD) calculated by error propagation (including instrumental precisions, and mono elemental concentration uncertainties).

For isotopic measurements, all seawater samples were treated in a clean laboratory to isolate the two elements of interest from the matrix using conventional liquid chromatography. For each of them, 1 ml of the seawater sample was evaporated to dryness in a Savillex beaker on a hot plate at 70°C. Additionally, international seawater standards (IAPSO and NASS 6) were processed in the same manner alongside our samples.

Sr was isolated using Sr-Spec resin (Eichrom, United States) using the protocol described in Pin et al. (2014). Sr isotopic composition of individual fluid samples was measured on a

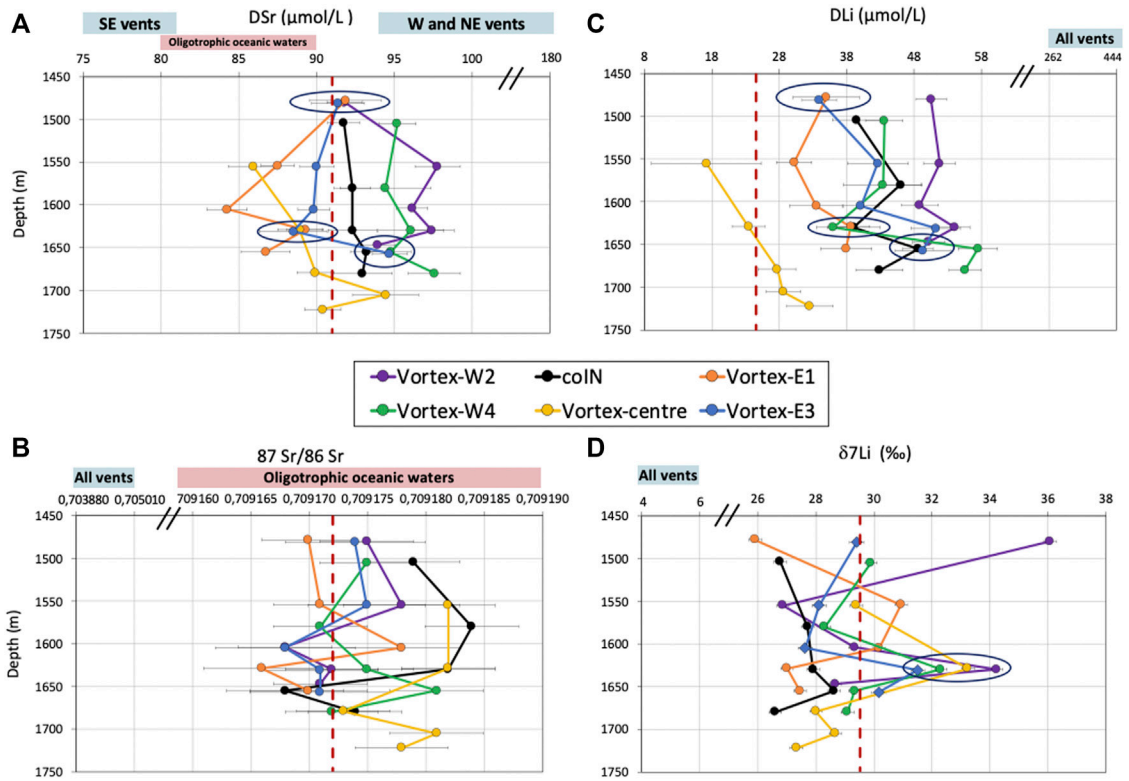

FIGURE 2 | Depth profiles of DSr (left panels) and DLi (right panels) elemental and isotopic compositions for the six CTD casts over the Lucky Strike Hydrothermal Field (LSHF). The data are all plotted with their respective uncertainties. Seawater compositions are indicated and correspond to **(A)** reference seawater (red dashed line at 91 µmol/L; Millero et al., 2008), and range of oligotrophic oceanic waters (red box between 80 and 90 µmol/L; El Meknassi et al., 2020), **(B)** the mean (red dashed line) and range (red box) of oligotrophic oceanic waters (0.709172 ± 0.000023; El Meknassi et al., 2020), and **(C, D)** IAPSO seawater standard composition (red dashed line at 24.6 µmol/L; Leleu, 2017; and at 29.5‰, this study). The hydrothermal fluid composition ranges of the LSHF vents (**Supplementary Table S2**) are indicated by the light blue boxes with the vent locations specified inside (SE = South East, W = West, NE = North East, All vents). Samples with identical elemental and/or isotopic compositions are circled.

Thermo Fisher Triton + Thermal Ionisation Mass Spectrometer at the Observatoire Midi-Pyrénées. The $^{87}Sr/^{86}Sr$ ratio was determined as the average values of 200 measurements of ion intensities following a static multi-collection mode. The $^{87}Sr/^{86}Sr$ ratios were corrected from mass fractionation based on the normalization value of $^{86}Sr/^{88}Sr$ ratio at 0.1194. The repeated measurements of the NBS 987 Sr standard gave a mean ratio of 0.710259 ± 0.000013 (2 SD; n = 24; 2SE = 0.000003) for a recommended value of 0.710250. The accuracy of our technique is verified against the $^{87}Sr/^{86}Sr$ ratios of international standards: 1. IAPSO seawater with a measured value of 0.709174 ± 0.000003 (2SD; n = 4), in line with the published values of 0.709179 ± 0.000007 (2SD; n = 7; El Meknassi et al., 2020), and 2. NASS-6 seawater with a measured value of 0.709174 ± 0.000005 (2SD; n = 3), in line with the published values of 0.709179 ± 0.000014 (2SD; n = 8; Neymark et al., 2014).

Li elution and isolation from the NaCl-rich matrix was carried out using two steps ion exchange columns made of AGW-X12 200–400 mesh cation resin bed and eluted with 1N HCl [Protocol adapted to NaCl-solution from James and Palmer (2000)]. Li isotopic composition of individual fluid samples was measured on a Thermo Fisher Triton + Thermal Ionisation Mass Spectrometer at the Observatoire Midi-Pyrénées. The Li samples were diluted with a freshly made 0.15 N H_3PO_4. 1 µL of the resulting solution (~30–60 ng of Li) was deposited on 1 µL of 0.15 N H_3PO_4 previously loaded on one side of a degassed double Re filament. After loading, the sample dried down gently at filament current at 0.8 A, then heated up to 2.4 A until acid phosphoric fumes were driven off, and then flashed at 2.8 A. During isotopic measurement, the current of the ionization filament was raised to ~2 A to reach a pyrometer temperature of ~1210–1220°C whereas the evaporation filament was increased to ~0.7–0.9 A until a stable ^{7}Li beam of ~5V was reached. The $^{7}Li/^{6}Li$ ratio was determined as the average values of 200 measurements of ion intensities following a static multi-collection mode. The $^{7}Li/^{6}Li$ ratios are expressed in a $\delta^{7}Li$‰ relative to the IRMM-16 Li standard (Li_2CO_3) at a similar Li concentration. The repeated measurements of the IRMM-16 standard gave a $^{7}Li/^{6}Li$ ratio mean of 12.08709 ± 0.01525 (2SD; n = 33), an internal precision of 0.22‰ (2SE, uncertainty reported on the error bars in **Figure 2**), and an external precision of 1.26‰ (2SD; n = 33). The accuracy of our technique is verified against the measured ratios of international IAPSO seawater standard with a measured value of +29.5 ± 0.2‰

(2SE), in line with the published values of +30.8 ± 0.1‰ (2SE, with external precision ≤1‰; Rosner et al. (2007)).

RESULTS

The Sr and Li elemental and isotopic compositions of the six CTD casts are reported in **Table 1** and presented as depth profiles in **Figure 2**.

Measured DSr concentrations range between 84 and 98 µmol/L at the six CTD casts (**Figure 2A**; **Table 1**). Variability of DSr concentrations is observed as a function of depth and cast location. Eastern casts (Vortex-E1 and -E3) mainly display DSr concentrations in agreement with oligotrophic oceanic water values at 80–90 µmol/L (red box in **Figure 2A**; El Meknassi et al. (2020)) but lower than the reference seawater concentration of 91 µmol/L (red dashed line in **Figure 2A**; Millero et al., 2008), whereas western casts (Vortex-W2 and -W4) exhibit higher concentrations. Dissolved Sr concentrations of water mass outside the LSHF, i.e., at the coIN cast, remain essentially constant throughout the depth profile, at ~92–93 µmol/L, at intermediate values between eastern and western DSr concentrations. Dissolved Sr concentrations at Vortex-centre are within the range of published oligotrophic oceanic waters (apart from one sample at 1705 mbsl). Surprisingly, a few samples have identical DSr concentrations at the same water depth whatever their locations within the LSHF, e.g., 1480, 1630, and 1660 mbsl (circled samples in **Figure 2A**). The differences observed in DSr concentrations between the western and eastern casts are not evidenced in their respective $^{87}Sr/^{86}Sr$ ratios. The measured $^{87}Sr/^{86}Sr$ ratios vary between 0.709166 and 0.709184 at the six CTD casts with a mean value of 0.709174 ± 0.000002 (2SD, n = 30, **Figure 2B**; **Table 1**). This value is coherent with the mean value of oligotrophic oceanic waters at 0.709172 ± 0.000023 (2SD, n = 84; red dashed line in **Figure 2B**; El Meknassi et al. (2018); El Meknassi et al. (2020)).

Measured DLi concentrations range between 17 and 57 µmol/L at the six CTD casts (**Figure 2C**; **Table 1**). As for DSr, DLi concentrations vary as a function of depth and casts location. Moreover, a few samples have identical DLi concentrations at the same water depths identified for DSr (the circled samples in **Figure 2C**). Vortex-centre samples exhibit DLi concentrations (17–33 µmol/L) the closest to seawater value (within analytical error) at 24.6 µmol/L (red dashed line in **Figure 2C**; Leleu (2017)), whereas all other casts are characterized by higher DLi concentrations by up to 133%. No clear DLi differences are observed between the eastern and western casts. The δ^7Li vary between +25.9 and +36.1‰ (**Figure 2D**; **Table 1**), extending and overlapping the previous δ^7Li values measured on different water masses of Pacific and Atlantic oceans (from +29.3 to +32.5‰; Sahoo and Masuda, 1998; Tomascak et al., 1999; Nishio and Nakai, 2002; Pistiner and Henderson, 2003; Millot et al., 2004, among others). At all casts except coIN and Vortex-E1, a heavy δ^7Li value (>+31‰) conjointly occurs at the same water depth of ~1630 mbsl (circled samples in **Figure 2D**). The heaviest δ^7Li value of +36.1‰ is obtained as a standalone value for Vortex-W2 cast at 1480 mbsl.

DISCUSSION

Hydrothermal Input of Strontium in the Water Column

The depth profiles of DSr (**Figure 2A**) are distinct from one cast to another as evidenced by 1) constant DSr at seawater value throughout coIN cast, 2) lower DSr concentrations than reference seawater on eastern casts (Vortex-E1 and -E3), and 3) higher DSr concentrations than seawater on western casts (Vortex-W2 and -W4). Regarding the coIN cast, its DSr values are close to the reference seawater value (dashed red line in **Figure 2A**) and its $^{87}Sr/^{86}Sr$ ratios fall within the range of oligotrophic oceanic waters (red box in **Figure 2B**), evidencing no detection of hydrothermal contribution at this location. **Figure 3** illustrates a 3D vision of all datasets at the LSHF scale. **Figure 3A** dedicated to DSr includes a 91 µmol/L isosurface representative of DSr reference seawater value (Millero et al., 2008), pointing out the opposite trends of DSr variability between the eastern and western casts. Indeed, the LSHF hosts about ~30 active hydrothermal vents distributed over its 1 km^2 surface area. At this location, Chavagnac et al. (2018a) and Leleu (2017) showed that high-temperature hydrothermal fluids contain DSr concentrations that are either lower or higher than seawater depending on the vent. In particular, the vents located on the western and north-eastern sides of the LSHF contain 94–179 µmol/L of DSr and all the south-eastern vents display 74–81 µmol/L of DSr (light blue boxes in **Figure 2A**, and **Supplementary Table S2**; Von Damm et al., 1998; Charlou et al., 2000; Pester et al., 2012; Chavagnac et al., 2018a). These features are in line with the DSr depletions observed for south-eastern casts at depth and the gradual increase toward the reference seawater value that is reached at 1480 mbsl. They are also in line with the DSr enrichments observed for western casts at depth and the gradual decrease toward the seawater value also reached at 1480 mbsl (**Figure 2A**). These trends reflect the progressive decreasing contribution of hydrothermal fluid to seawater and the lighter ventilation by hydrothermal plumes of distant water above the seafloor. Clearly, the DSr dataset shows the hydrothermal contribution to the water column, considering the specific chemical characteristics of each vent, which can be tracked up to ~300 m above the seafloor. This hydrothermal impact cannot be so easily detected from $^{87}Sr/^{86}Sr$ ratios of all datasets, as illustrated by the data profiles (**Figure 2B**) and the 3D representation (**Figure 3B**). The highest $^{87}Sr/^{86}Sr$ ratio difference is obtained at 1630 mbsl between coIN/Vortex-centre and Vortex-E1 with the values of 0.709182 ± 0.000004 and 0.709166 ± 0.000005, respectively (**Table 1**). Even if this ratio difference is significant compared to the internal precision (±2SE = 0.000003), the mean value of all casts is 0.709174 ± 0.000010 (±2SD; n = 30), which falls within the range of oligotrophic oceanic waters at 0.709172 ± 0.000023 (±2SD, n = 84; global scale; El Meknassi et al., 2020). Thus, the Sr

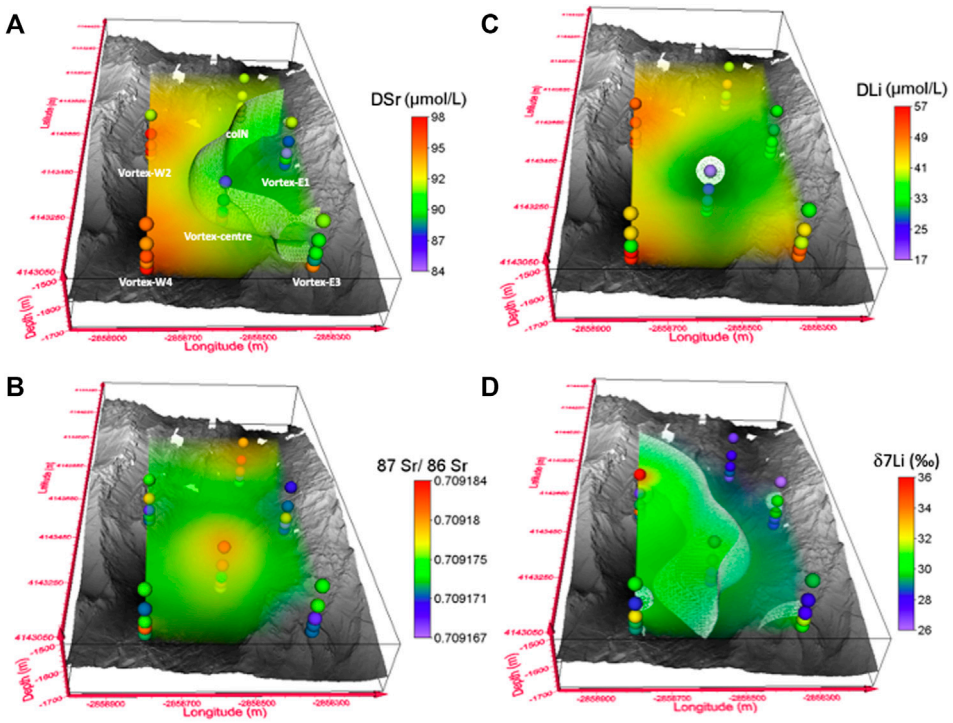

FIGURE 3 | Dissolved Sr and Li concentrations [**(A)** and **(C)**, respectively] and isotopic compositions [**(B)** and **(D)**, respectively] are presented as a 3D scatter plot over the LSHF bathymetric map. The dispersion of the data points is simulated with volume rendering. The isosurfaces are fixed at the seawater composition, i.e., **(A)** 91 µmol/L for DSr (Millero et al., 2008), **(C)** 24.6 µmol/L for DLi (Leleu, 2017), and **(D)** 29.5‰ for δ^7Li (this study).

isotopic system does not allow the detection of hydrothermal plume input in the water column at the LSHF km-scale. However, this does not mean that the hydrothermal input in the water column could not be detected with the Sr isotopic system at a smaller scale (e.g., m-scale). Only additional studies at an m-scale could answer this question.

Hydrothermal Input of Lithium in the Water Column

The DLi dataset is represented as depth profiles (**Figure 2C**) and as a 3D vision (**Figure 3C**), including the seawater DLi isosurface (24.6 µmol/L). The depth profiles of DLi present the following features: 1) higher DLi concentrations than seawater at all casts and depths apart from Vortex-centre, 2) no clear DLi differences between the eastern and western casts, and 3) DLi concentrations increase at depth at all casts except coIN and Vortex-W2. Among all the CTD casts performed at the LSHF, Vortex-centre is the only one displaying DLi concentrations close to the seawater value (**Figure 2C**), whereas all the others are enriched by 23–133%. High-temperature hydrothermal fluids are 10–20 times more enriched in DLi (287–398 µmol/L) than seawater without any distinction between the eastern and western sites (light blue box in **Figure 2C**; **Supplementary Table S2**; Leleu, 2017; Chavagnac et al., 2018a). The DLi enrichment seen in CTD casts can result from a hydrothermal contribution to the water column by up to 10% considering a DLi conservative behavior. A hydrothermal source of DLi to the water column can be further sustained, especially at Vortex-E3 and Vortex-W4, by the sharp DLi increase at depth up to 10 and 21 µmol/L, respectively (deeper than 1600 mbsl, **Figure 2C**). Then, as for DSr, hydrothermal contribution to the water column can be detected by measuring DLi concentrations of CTD casts on the LSHF km-scale and up to ~300 m above the seafloor.

Previous δ^7Li values measured on different water masses collected in Pacific and Atlantic oceans range between +29.3 and +32.5‰ (**Figure 2D**; James and Palmer, 2000; Nishio and Nakai, 2002, among others). Moreover, the signatures of the different water masses in the Atlantic Ocean are not precisely defined contrarily to other isotopic systems such as neodymium isotopes (Lacan and Jeandel, 2005; Hartman, 2015). Our δ^7Li dataset will then be compared to that of the IAPSO seawater standard supplied and prepared from natural mid-Atlantic surface waters, and therefore, outside any hydrothermal influence (Bacon et al., 2007). Our measured δ^7Li value of IAPSO is +29.5 ± 0.2‰ (±2SE). Taking this value as a reference for seawater, δ^7Li values of all CTD casts are lower, equal, and higher, i.e., from +25.9 to +36.1‰ (**Table 1**; **Figures 2D**, **3D**). Regarding LSHF hydrothermal fluids, δ^7Li values range from +4.4 to +6.4‰ with a mean value of 5.4 ± 0.9‰ (2SD, n = 26; Leleu, 2017, and references therein). As a result, any hydrothermal input to the water column at LSHF should be evidenced by δ^7Li values lower than that of seawater, if no additional fractionation processes are at play.

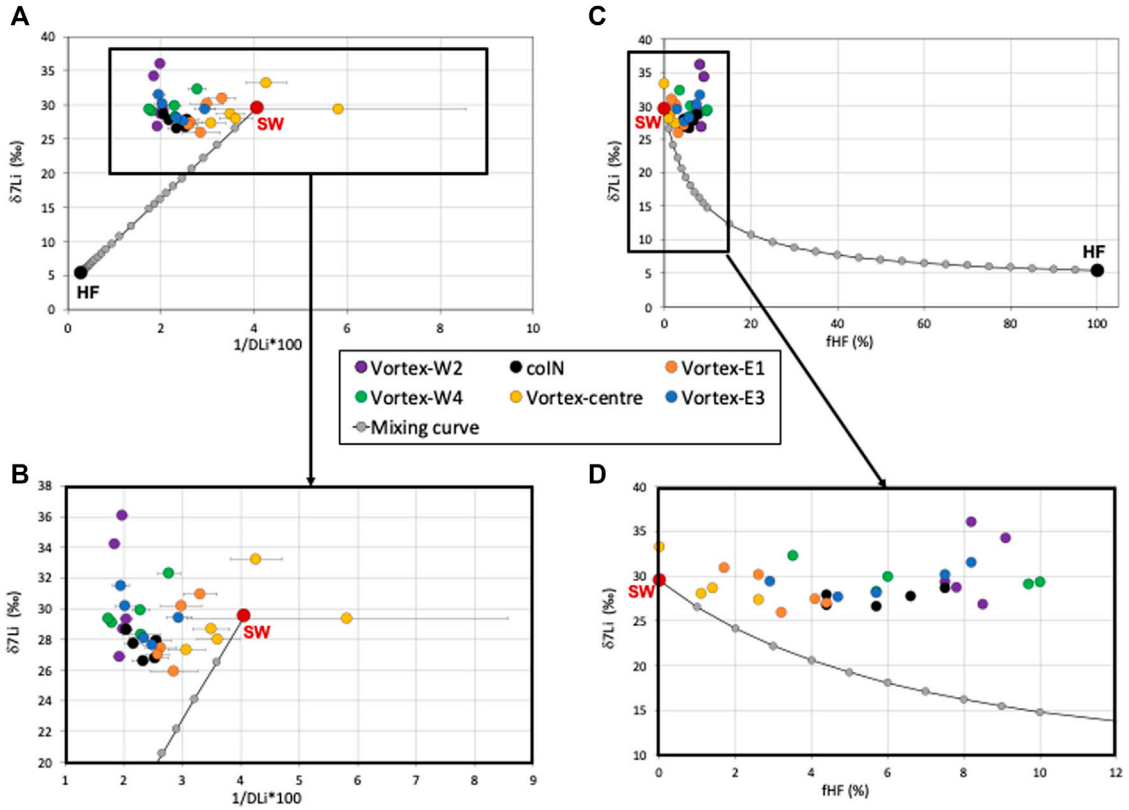

FIGURE 4 | Variations of **(A, B)** δ^7Li values as a function of 1/DLi*100 for the six CTD casts, and **(C, D)** δ^7Li values as a function of hydrothermal fluid contribution calculated considering a conservative DLi behavior (fHF%). For the four plots, a conservative mixing trend between seawater and hydrothermal fluid end-members is reported as gray dots. Seawater (SW, red dot), and hydrothermal fluid (HF, black dot) end-members are indicated.

Figure 4A presents the δ^7Li values as a function of 1/DLi*100 to scrutinize and discriminate between hydrothermal contribution to seawater and isotopic fractionation processes. The mixing between hydrothermal fluid and seawater involves physicochemical gradients that lead to mineral precipitation (sulfate-bearing minerals, polymetallic sulfides, iron oxyhydroxides, and manganese oxides) which can be further dissolved and reprecipitated in the buoyant to the non-buoyant hydrothermal plume (Chavagnac et al., 2018b; Lee et al., 2021). Such mineral—seawater interactions (mineral precipitation and dissolution, element adsorption) can induce Li isotope fractionation, i.e., the preferential adsorption of ^{6}Li over ^{7}Li on mineral (Decitre et al., 2004; Chan and Hein, 2007; Vigier et al., 2008; Araoka et al., 2016; Wilckens et al., 2019). The δ^7Li and DLi datasets of all casts do not follow the conservative mixing curve between hydrothermal fluid and seawater end-members (**Figures 4A,B**). However, the DLi versus DSr concentrations define a linear trend (**Supplementary Figure S1**), suggesting that conservative mixing occurs between these two end-members. Moreover, high DLi concentration (discussed above) necessarily involves a DLi source that at the LSHF location is most likely of hydrothermal origin. Therefore, we can calculate the hydrothermal fluid contribution to the water column for all samples considering a DLi conservative behavior (fHF column in **Table 1**). **Figures 4C,D** presents the δ^7Li values as a function of the fraction of hydrothermal fluid (fHF expressed in %). The difference between the δ^7Li signatures of our samples and the mixing curve becomes larger as fHF increases (**Figures 4C,D**). In other words, the δ^7Li signatures of our samples become heavier as the hydrothermal fluid contribution increases. Thus, the main effects impacting the LSHF water column are DLi input of hydrothermal fluid leading to heavy δ^7Li values. We hypothesize that these positive deviations from conservative mixing are due to mineral—seawater interactions. This has already been evidenced in buoyant hydrothermal fluids along the mixing gradient where anhydrite/baryte precipitation and dissolution disrupt dissolved rare-earth element concentrations and neodymium isotopic compositions (Chavagnac et al., 2018b). Regarding hydrothermal lithium, Chan and Hein (2007) showed that the hydrated form of Li (LiOH) can be adsorbed preferentially on negatively charged surfaces of Mn oxides contrarily to positively charged surfaces of Fe oxy-hydroxides. The preferential adsorption of ^{6}Li over ^{7}Li on hydrothermal minerals is evidenced in our dataset by the heaviest δ^7Li measured on water samples with the highest hydrothermal contribution. However, Chan and Hein (2007) showed that Li adsorbed on Mn oxides surface continuously exchanges its Li isotopes with those of seawater, losing its original hydrothermal

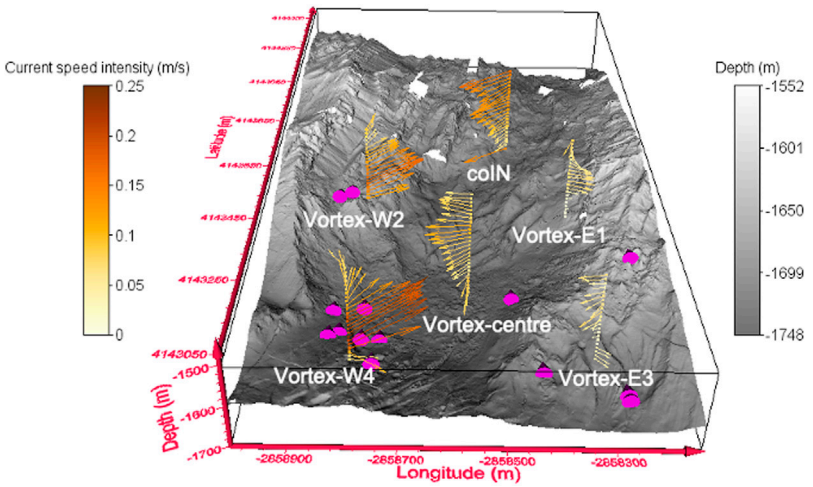

FIGURE 5 | Profiles of current speed intensities and direction (acquired *via* ADCP) at the six CTD casts reported on the top of 3D bathymetric map of the Lucky strike hydrothermal field. Active hydrothermal vents are indicated by pink cones. Refer to **Supplementary Table S3** for current intensity values and to **Supplementary Figure S2** for another current profiles representation.

δ^7Li signature. This progressive re-equilibration toward δ^7Li seawater signature is observed in our samples with decreasing hydrothermal contribution (**Figures 4C,D**).

The Effect of Current Dynamics on Hydrothermal Plume Dispersion

At the km-scale LSHF, hydrothermal input can be tracked in the water column using Sr and Li elemental concentrations up to ~300 m above the seafloor. At depth, the variations of DSr and DLi depict the influence of hydrothermal fluids with their specific chemical characteristics. Further processes such as hydrothermal contribution and mineral-seawater interactions can be detected by δ^7Li signature once combined with DLi concentrations. We anticipate that the closer the CTD cast is to a hydrothermal source, the stronger the influence of hydrothermal inputs on the water samples. This explanation is overall in agreement with our dataset. Nevertheless and surprisingly, some geographically distant CTD casts with different element profiles display identical DSr and DLi concentrations or similar δ^7Li signatures at the same depth, e.g., in particular at 1630 mbsl (**Figures 2A,C,D**). Moreover, the coIN cast located at the northern edge of the fossil lava lake and outside the immediate influence of LSHF show high DLi concentrations (between 39 and 49 µmol/L; **Figure 2C**) and lower δ^7Li signatures compared with seawater (between 26.6 and 28.6‰, **Figure 2D**). Then, although coIN could be considered the most representative of seawater composition based on its DSr concentrations and ^{87}Sr/^{86}Sr ratios (**Table 1**; **Figures 2A,B**), its Li signatures suggest hydrothermal contribution present up to 1480 mbsl. The Sr and Li results contradict each other, therefore questioning the eventual occurrence of an active hydrothermal vent in the vicinity of the coIN cast. The only available Sr and Li data for the LSHF northwestern area are for the Jason (in 1996, Von Damm et al., 1998) and Elisabeth (in 2008, Pester et al., 2012) sites prior to their sampling exclusion as part of the Lucky Strike Marine Protected area (Mullineaux et al., 1998; Leleu, 2017). Without further investigation in this area, the occurrence of an active hydrothermal site remains an open question. At LSHF, hydrothermal vents are distributed around a fossil lava lake, which is surrounded by three ancient volcanic cones (Ondréas et al., 2009). This peculiar topography can constrain the current dynamics in the lava lake and produce specific dispersion patterns. Moreover, the injection of high-temperature hydrothermal fluids (up to 360°C) in a cold seawater mass (~4°C) may contribute to the formation of currents at depth (Dutay et al., 2004).

Figure 5 presents the spatial variations in the direction and intensity of oceanic currents at the six CTD casts as measured by the LADCPs (current intensity values available in **Supplementary Table S3**). Currents vary from one cast to the other, are stronger at the LSHF western side (up to 0.25 m/s at Vortex-W4), and show variable direction from the bottom up to 1450 mbsl. Western casts (Vortex-W2 and -W4) display their maximum current speed intensities up to 0.17 m/s and 0.25 m/s, respectively, between 1560 and 1650 mbsl with a general North East direction (**Figure 5**; **Supplementary Figure S2**). On the contrary, eastern casts as well as Vortex-Centre display their maximum current intensities (from 0.07 to 0.17 m/s) at 1450 mbsl toward the SW direction. Given the small size of the lava lake (1 km^2) and the intensity of the measured currents, the hydrothermal signature of the western part of the lake can easily be advected toward the center and eastern parts in less than an hour (for a current intensity of 0.25 m/s). This may explain why CTD casts distanced from one another by less than a km can exhibit similar and/or identical Sr and Li elemental and isotopic signatures.

Resing et al. (2015) showed that the dispersion of hydrothermal input can be tracked in the water column up to 4,000 km away from its source using dFe concentrations, i.e., Fe has a short residence time in the ocean (200–500 yr; Millero, 1996; Johnson et al., 1997). While Sr and Li have a much longer

residence time than Fe, i.e., 2–3 Myr (Hodell et al., 1990; Millero, 1996), we show that hydrothermal input can be detected with these tracers at a km-scale investigation. This suggests that chemical tracers of hydrothermal input have to be chosen depending on the spatial scale of the studied area.

CONCLUSION

Here, we investigate hydrothermal DLi and DSr dispersion in the water column over the LSHF. The data were acquired on 30 seawater column samples collected between 1478 and 1722 mbsl at five CTD casts distributed over the LSHF and one at its northern border.

Both DSr and DLi concentrations vary as a function of depth and cast location. Values are different and distinctive from seawater, and reflect the local influence of hydrothermal input up to 1478 mbsl considering the specific chemical characteristics of hydrothermal sources. Moreover, an overall DLi enrichment occurs which can be attributed to a 10% hydrothermal contribution to the water column, based on a conservative DLi behavior. However, heavy δ^7Li signatures cannot be explained by a conservative mixing between seawater and hydrothermal fluid end-members for increasing hydrothermal input. We invoke the mineral–seawater interaction process that leads to preferential ^{6}Li adsorption over ^{7}Li on Mn oxides surface, coherent with the observed heaviest δ^7Li values in the water column.

Regarding the current dynamics above the LSHF, the hydrothermal signature preserved in the western part of the lake can easily be advected toward the center and eastern parts in less than 1 h at the LSHF km-scale. This may explain why geographically distant CTD casts with different element profiles display at certain depth identical DSr and DLi concentrations or similar δ^7Li signatures.

At a km-scale investigation, hydrothermal input to the water column can be detected up to 300 m above the seafloor using DSr and DLi elemental and isotopic compositions. Regarding ^{87}Sr/^{86}Sr ratios, they fall within the oligotrophic oceanic waters range. Nevertheless, the variability between the samples is significant compared to the internal analytical precision, suggesting its potential use as a hydrothermal tracer at an m-scale investigation.

DATA AVAILABILITY STATEMENT

The original contributions presented in the study are included in the article/**Supplementary Material**, further inquiries can be directed to the corresponding author.

AUTHOR CONTRIBUTIONS

VC, CD, BF, and CC collected the samples on board of the Momarsat'19 cruise. BF processed the CTD and LADCP data. LA, VC, and CD designed the study. LA performed the elemental and isotopic analyses, the formal analysis, organized the database, and performed the visualization/data presentation work. LA, VC, and CD conducted the interpretation work and drafted the manuscript with contributions from BF and CC.

FUNDING

The Institut Carnot ISIFoR through the ADERA provided funding for LA, and VC. The CNRS/INSU TELLUS 2021 call provided funding for the AMINO project. The EU project ERIC—EMSO (http://www.emso-eu.org/) provided funding for the maintenance of the EMSO-Azores observatory. Isblue provided funding for CC.

ACKNOWLEDGMENTS

We thank the *R.V. Pourquoi Pas?* and Genavir crew for their tremendous work during the MoMARsat'19. We thank Olivier Peden, Guillaume Roullet, and Noé Lahaye for the CTD/LADCP preparation and operations at sea. We are grateful to the chemistry facility of the Géoscience Environment Toulouse laboratory (GET), the clean room facility of the Laboratoire d'Etudes en Geophysique et Océanographie Spatiales (LEGOS), and the mass spectrometry facility of the PANGEE platform at the Observatoire Midi-Pyrénées (OMP). All geochemical measurements made on board the 2013, 2014, 2015, and 2019 MoMARsat cruises are available in their cruise report at the following DOIs: https://doi.org/10.17600/13030040, https://doi.org/10.17600/14000300, https://doi.org/10.17600/15000200, and https://doi.org/10.17600/18001110, respectively. The pure hydrothermal fluid measurements presented in this paper are available at the following HAL Id: tel-01874701. We acknowledge the comments of two reviewers which improved the quality of the manuscript.

SUPPLEMENTARY MATERIAL

The Supplementary Material for this article can be found online at: https://www.frontiersin.org/articles/10.3389/fenvc.2022.784385/full#supplementary-material

REFERENCES

Albarède, F., Michard, A., Minster, J. F., and Michard, G. (1981). 87Sr/86Sr Ratios in Hydrothermal Waters and Deposits from the East Pacific Rise at 21°N. *Earth Planet. Sci. Lett.* 55 (2), 229–236. doi:10.1016/0012-821X(81)90102-3

Allègre, C. J., Louvat, P., Gaillardet, J., Meynadier, L., Rad, S., and Capmas, F. (2010). The Fundamental Role of Island Arc Weathering in the Oceanic Sr Isotope Budget. *Earth Planet. Sci. Lett.* 292 (1–2), 51–56. doi:10.1016/j.epsl.2010.01.019

Andrews, E., Pogge von Strandmann, P. A. E., and Fantle, M. S. (2020). Exploring the Importance of Authigenic clay Formation in the Global Li Cycle. *Geochimica et Cosmochimica Acta* 289, 47–68. doi:10.1016/j.gca.2020.08.018

Araoka, D., Nishio, Y., Gamo, T., Yamaoka, K., and Kawahata, H. (2016). Lithium Isotopic Systematics of Submarine Vent Fluids from Arc and Back-Arc

Hydrothermal Systems in the Western Pacific. *Geochem. Geophys. Geosyst.* 17 (10), 3835–3853. doi:10.1002/2016GC006355

Bacon, S., Culkin, F., Higgs, N., and Ridout, P. (2007). IAPSO Standard Seawater: Definition of the Uncertainty in the Calibration Procedure, and Stability of Recent Batches. *J. Atmos. Oceanic Tech.* 24 (10), 1785–1799. doi:10.1175/JTECH2081.1

Barker, A. K., Coogan, L. A., Gillis, K. M., and Weis, D. (2008). Strontium Isotope Constraints on Fluid Flow in the Sheeted dike Complex of Fast Spreading Crust: Pervasive Fluid Flow at Pito Deep. *Geochem. Geophys. Geosystems* 9 (6), 1–19. doi:10.1029/2007gc001901

Beck, A. J., Charette, M. A., Cochran, J. K., Gonneea, M. E., and Peucker-Ehrenbrink, B. (2013). Dissolved Strontium in the Subterranean Estuary - Implications for the marine Strontium Isotope Budget. *Geochimica et Cosmochimica Acta* 117, 33–52. doi:10.1016/j.gca.2013.03.021

Besson, P., Degboe, J., Berge, B., Chavagnac, V., Fabre, S., and Berger, G. (2014). Calcium, Na, K and Mg Concentrations in Seawater by Inductively Coupled Plasma-Atomic Emission Spectrometry: Applications to IAPSO Seawater Reference Material, Hydrothermal Fluids and Synthetic Seawater Solutions. *Geostand Geoanal Res.* 38 (3), 355–362. doi:10.1111/j.1751-908X.2013.00269.x

Bickle, M. J., and Teagle, D. A. H. (1992). Strontium Alteration in the Troodos Ophiolite: Implications for Fluid Fluxes and Geochemical Transport in Mid-ocean ridge Hydrothermal Systems. *Earth Planet. Sci. Lett.* 113 (1), 219–237. doi:10.1016/0012-821X(92)90221-G

Brunskill, G. J., Zagorskis, I., and Pfitzner, J. (2003). Geochemical Mass Balance for Lithium, boron, and Strontium in the Gulf of Papua, Papua New Guinea (Project TROPICS). *Geochimica et Cosmochimica Acta* 67 (18), 3365–3383. doi:10.1016/S0016-7037(02)01410-2

Chan, L.-H., and Hein, J. R. (2007). Lithium Contents and Isotopic Compositions of Ferromanganese Deposits from the Global Ocean. *Deep Sea Res. Part Topical Stud. Oceanography* 54 (11), 1147–1162. doi:10.1016/j.dsr2.2007.04.003

Charlou, J. L., Donval, J. P., Douville, E., Jean-Baptiste, P., Radford-Knoery, J., Fouquet, Y., et al. (2000). Compared Geochemical Signatures and the Evolution of Menez Gwen (37°50′N) and Lucky Strike (37°17′N) Hydrothermal Fluids, South of the Azores Triple Junction on the Mid-Atlantic Ridge. *Chem. Geology.* 171 (1), 49–75. doi:10.1016/S0009-2541(00)00244-8

Chavagnac, V., Leleu, T., Fontaine, F., Cannat, M., Ceuleneer, G., and Castillo, A. (2018a). Spatial Variations in Vent Chemistry at the Lucky Strike Hydrothermal Field, Mid-Atlantic Ridge (37°N): Updates for Subseafloor Flow Geometry from the Newly Discovered Capelinhos Vent. *Geochem. Geophys. Geosyst.* 19 (11), 4444–4458. doi:10.1029/2018GC007765

Chavagnac, V., Saleban Ali, H., Jeandel, C., Leleu, T., Destrigneville, C., Castillo, A., et al. (2018b). Sulfate Minerals Control Dissolved Rare Earth Element Flux and Nd Isotope Signature of Buoyant Hydrothermal Plume (EMSO-Azores, 37°N Mid-Atlantic Ridge). *Chem. Geology.* 499, 111–125. doi:10.1016/j.chemgeo.2018.09.021

Colaço, A., Blandin, J., Cannat, M., Carval, T., Chavagnac, V., Connelly, D., et al. (2011). MoMAR-D: A Technological challenge to Monitor the Dynamics of the Lucky Strike Vent Ecosystem. *ICES J. Mar. Sci.* 68 (2), 416–424. doi:10.1093/icesjms/fsq075

Davis, A. C., Bickle, M. J., and Teagle, D. A. H. (2003). Imbalance in the Oceanic Strontium Budget. *Earth Planet. Sci. Lett.* 211 (1), 173–187. doi:10.1016/S0012-821X(03)00191-2

Decitre, S., Buatier, M., and James, R. (2004). Li and Li Isotopic Composition of Hydrothermally Altered Sediments at Middle Valley, Juan De Fuca. *Chem. Geology.* 211 (3), 363–373. doi:10.1016/j.chemgeo.2004.07.005

Dutay, J.-C., Jean-Baptiste, P., Campin, J.-M., Ishida, A., Maier-Reimer, E., Matear, R. J., et al. (2004). Evaluation of OCMIP-2 Ocean Models' Deep Circulation with Mantle Helium-3. *J. Mar. Syst.* 48 (1), 15–36. doi:10.1016/j.jmarsys.2003.05.010

Ehya, F., Shakouri, B., and Rafi, M. (2013). Geology, Mineralogy, and Isotope (Sr, S) Geochemistry of the Likak Celestite deposit, SW Iran. *Carbonates Evaporites* 28 (4), 419–431. doi:10.1007/s13146-013-0137-6

El Meknassi, S., Dera, G., Cardone, T., De Rafélis, M., Brahmi, C., and Chavagnac, V. (2018). Sr Isotope Ratios of Modern Carbonate Shells: Good and Bad News for Chemostratigraphy. *Geology* 46 (11), 1003–1006. doi:10.1130/G45380.1

El Meknassi, S., Dera, G., De Rafélis, M., Brahmi, C., Lartaud, F., Hodel, F., et al. (2020). Seawater 87Sr/86Sr Ratios along continental Margins: Patterns and Processes in Open and Restricted Shelf Domains. *Chem. Geology.* 558, 119874. doi:10.1016/j.chemgeo.2020.119874

Escartin, J., Barreyre, T., Cannat, M., Garcia, R., Gracias, N., Deschamps, A., et al. (2015). Hydrothermal Activity along the Slow-Spreading Lucky Strike ridge Segment (Mid-Atlantic Ridge): Distribution, Heatflux, and Geological Controls. *Earth Planet. Sci. Lett.* 431, 173–185. doi:10.1016/j.epsl.2015.09.025

European Commission (2012). *Blue Growth Opportunities for marine and Maritime Sustainable Growth, Communication From the Commission to the European Parliament, the council, the European Economic and Social Committee and the Committee of the Regions* (Policy Document COM(2012) 494 Final). Available at: https://eur-lex.europa.eu/legal-content/EN/TXT/PDF/?uri=CELEX:52012DC0494&from=EN (Accessed September 15, 2021).

European Commission (2020). Study on the EU's List of Critical Raw Materials – Final Report. Available at: https://eur-lex.europa.eu/legal-content/EN/TXT/PDF/?uri=CELEX:52020DC0474&from=EN (Accessed September 15, 2021).

Fouquet, Y., Ondréas, H., Charlou, J.-L., Donval, J.-P., Radford-Knoery, J., Costa, I., et al. (1995). Atlantic Lava Lakes and Hot Vents. *Nature* 377 (6546), 201. doi:10.1038/377201a0

Gruber, P. W., Medina, P. A., Keoleian, G. A., Kesler, S. E., Everson, M. P., and Wallington, T. J. (2011). Global Lithium Availability: A Constraint For Electric Vehicles? *J. Ind. Ecol.* 15 (5), 760–775. doi:10.1111/j.1530-9290.2011.00359.x

Guieu, C., Bonnet, S., Petrenko, A., Menkes, C., Chavagnac, V., Desboeufs, K., et al. (2018). Iron from a Submarine Source Impacts the Productive Layer of the Western Tropical South Pacific (WTSP). *Sci. Rep.* 8 (1), 9075. doi:10.1038/s41598-018-27407-z

Hartman, A. E. (2015). *The Neodymium Composition of Atlantic Ocean Water Masses: Implications for the Past and Present*. New York: Columbia University. doi:10.7916/D8DZ077F

Hodell, D. A., Mead, G. A., and Mueller, P. A. (1990). Variation in the Strontium Isotopic Composition of Seawater (8 Ma to Present) : Implications for Chemical Weathering Rates and Dissolved Fluxes to the Oceans. *Chem. Geology. Isotope Geosci. Section* 80 (4), 291–307. doi:10.1016/0168-9622(90)90011-Z

Hong, H.-J., Park, I.-S., Ryu, T., Jeong, H. S., and Ryu, J. (2018). Demonstration of Seawater Strontium (Sr(II)) Extraction and Enrichment by a Biosorption Technique through Continuous Column Operation. *Ind. Eng. Chem. Res.* 57 (38), 12909–12915. doi:10.1021/acs.iecr.8b02895

Huh, Y., Chan, L.-H., Zhang, L., and Edmond, J. M. (1998). Lithium and its Isotopes in Major World Rivers: Implications for Weathering and the Oceanic Budget. *Geochimica et Cosmochimica Acta* 62 (12), 2039–2051. doi:10.1016/S0016-7037(98)00126-4

James, R. H., and Palmer, M. R. (2000). The Lithium Isotope Composition of International Rock Standards. *Chem. Geology.* 166 (3–4), 319–326. doi:10.1016/S0009-2541(99)00217-X

Johnson, K. S., Gordon, R. M., and Coale, K. H. (1997). What Controls Dissolved Iron Concentrations in the World Ocean? *Mar. Chem.* 57 (3), 137–161. doi:10.1016/S0304-4203(97)00043-1

Jones, M. T., Gislason, S. R., Burton, K. W., Pearce, C. R., Mavromatis, V., Pogge von Strandmann, P. A. E., et al. (2014). Quantifying the Impact of Riverine Particulate Dissolution in Seawater on Ocean Chemistry. *Earth Planet. Sci. Lett.* 395, 91–100. doi:10.1016/j.epsl.2014.03.039

Jones, M. T., Pearce, C. R., Jeandel, C., Gislason, S. R., Eiriksdottir, E. S., Mavromatis, V., et al. (2012b). Riverine Particulate Material Dissolution as a Significant Flux of Strontium to the Oceans. *Earth Planet. Sci. Lett.* 355-356 (356), 51–59. doi:10.1016/j.epsl.2012.08.040

Jones, M. T., Pearce, C. R., and Oelkers, E. H. (2012a). An Experimental Study of the Interaction of Basaltic Riverine Particulate Material and Seawater. *Geochimica et Cosmochimica Acta* 77, 108–120. doi:10.1016/j.gca.2011.10.044

Kavanagh, L., Keohane, J., Garcia Cabellos, G., Lloyd, A., and Cleary, J. (2018). Global Lithium Sources-Industrial Use and Future in the Electric Vehicle Industry: A Review. *Resources* 7 (3), 57. doi:10.3390/resources7030057

Krabbenhöft, A., Eisenhauer, A., Böhm, F., Vollstaedt, H., Fietzke, J., Liebetrau, V., et al. (2010). Constraining the marine Strontium Budget with Natural Strontium Isotope Fractionations ($^{87}Sr/^{86}Sr*$, $\delta^{88}/^{86}Sr$) of Carbonates, Hydrothermal Solutions and River Waters. *Geochimica Et Cosmochimica Acta* 74 (14), 4097–4109. doi:10.1016/j.gca.2010.04.009

Lacan, F., and Jeandel, C. (2005). Acquisition of the Neodymium Isotopic Composition of the North Atlantic Deep Water. *Geochem. Geophys. Geosystems* 6 (12), 1–20. doi:10.1029/2005gc000956

Langmuir, C., Humphris, S., Fornari, D., Van Dover, C., Von Damm, K., Tivey, M. K., et al. (1997). Hydrothermal Vents Near a Mantle Hot Spot: The Lucky Strike Vent Field at 37°N on the Mid-Atlantic Ridge. *Earth Planet. Sci. Lett.* 148 (1–2), 69–91. doi:10.1016/S0012-821X(97)00027-7

Lee, J.-M., Lam, P. J., Vivancos, S. M., Pavia, F. J., Anderson, R. F., Lu, Y., et al. (2021). Changing Chemistry of Particulate Manganese in the Near- and Far-Field Hydrothermal Plumes from 15°S East Pacific Rise and its Influence on Metal Scavenging. *Geochimica et Cosmochimica Acta* 300, 95–118. doi:10.1016/j.gca.2021.02.020

Leleu, T. (2017). *Variabilité spatio-temporelle de la composition des fluides hydrothermaux (observatoire fond de mer EMSO-Açores, Lucky Strike): Traçage de la circulation hydrothermale et quantification des flux chimiques associés*. Toulouse: UT3 Paul Sabatier.

Mayfield, K. K., Eisenhauer, A., Santiago Ramos, D. P., Higgins, J. A., Horner, T. J., Auro, M., et al. (2021). Groundwater Discharge Impacts marine Isotope Budgets of Li, Mg, Ca, Sr, and Ba. *Nat. Commun.* 12 (1), 148. doi:10.1038/s41467-020-20248-3

Measures, C., Hatta, M., Fitzsimmons, J., and Morton, P. (2015). Dissolved Al in the Zonal N Atlantic Section of the US GEOTRACES 2010/2011 Cruises and the Importance of Hydrothermal Inputs. *Deep Sea Res. Part Topical Stud. Oceanography* 116, 176–186. doi:10.1016/j.dsr2.2014.07.006

Millero, F. J. (1996). *Chemical Oceanography*. Second Edition. Boca Raton: CRC Press.

Millero, F. J., Feistel, R., Wright, D. G., and McDougall, T. J. (2008). The Composition of Standard Seawater and the Definition of the Reference-Composition Salinity Scale. *Deep Sea Res. Oceanographic Res. Pap.* 55 (1), 50–72. doi:10.1016/j.dsr.2007.10.001

Millot, R., Guerrot, C., and Vigier, N. (2004). Accurate and High-Precision Measurement of Lithium Isotopes in Two Reference Materials by MC-ICP-MS. *Geostand Geoanalyt Res.* 28 (1), 153–159. doi:10.1111/j.1751-908X.2004.tb01052.x

Millot, R., Scaillet, B., and Sanjuan, B. (2010). Lithium Isotopes in Island Arc Geothermal Systems: Guadeloupe, Martinique (French West Indies) and Experimental Approach. *Geochimica et Cosmochimica Acta* 74 (6), 1852–1871. doi:10.1016/j.gca.2009.12.007

Mullineaux, L., Juniper, S. K., and Desbruyères, D. (1998). Deep-sea Sanctuaries at Hydrothermal Vents: A Position Paper. *InterRidge News* 7 (1), 15–16.

Neymark, L. A., Premo, W. R., Mel'nikov, N. N., and Emsbo, P. (2014). Precise Determination of δ^{88}Sr in Rocks, Minerals, and Waters by Double-Spike TIMS: a Powerful Tool in the Study of Geological, Hydrological and Biological Processes. *J. Anal. At. Spectrom.* 11, 65–75. doi:10.1039/c3ja50310k

Nishio, Y., and Nakai, S. I. (2002). Accurate and Precise Lithium Isotopic Determinations of Igneous Rock Samples Using Multi-Collector Inductively Coupled Plasma Mass Spectrometry. *Analytica Chim. Acta* 456 (2), 271–281. doi:10.1016/S0003-2670(02)00042-9

Ondréas, H., Cannat, M., Fouquet, Y., Normand, A., Sarradin, P. M., and Sarrazin, J. (2009). Recent Volcanic Events and the Distribution of Hydrothermal Venting at the Lucky Strike Hydrothermal Field, Mid-Atlantic Ridge. *Geochem. Geophys. Geosyst.* 10 (2), 1–18. doi:10.1029/2008GC002171

Palmer, M. R., and Edmond, J. M. (1989). The Strontium Isotope Budget of the Modern Ocean. *Earth Planet. Sci. Lett.* 92 (1), 11–26. doi:10.1016/0012-821X(89)90017-4

Pearce, C. R., Parkinson, I. J., Gaillardet, J., Charlier, B. L. A., Mokadem, F., and Burton, K. W. (2015). Reassessing the Stable (δ88/86Sr) and Radiogenic (87Sr/86Sr) Strontium Isotopic Composition of marine Inputs. *Geochimica et Cosmochimica Acta* 157, 125–146. doi:10.1016/j.gca.2015.02.029

Pester, N. J., Reeves, E. P., Rough, M. E., Ding, K., Seewald, J. S., and Seyfried, W. E. (2012). Subseafloor Phase Equilibria in High-Temperature Hydrothermal Fluids of the Lucky Strike Seamount (Mid-Atlantic Ridge, 37°17′N). *Geochimica et Cosmochimica Acta* 90, 303–322. doi:10.1016/j.gca.2012.05.018

Peucker-Ehrenbrink, B., and Fiske, G. J. (2019). A continental Perspective of the Seawater 87Sr/86Sr Record: A Review. *Chem. Geology.* 510, 140–165. doi:10.1016/j.chemgeo.2019.01.017

Pin, C., Gannoun, A., and Dupont, A. (2014). Rapid, Simultaneous Separation of Sr, Pb, and Nd by Extraction Chromatography Prior to Isotope Ratios Determination by TIMS and MC-ICP-MS. *J. Anal. Spectrom.* 29, 1858–1870. doi:10.1039/C4JA00169A

Pistiner, J. S., and Henderson, G. M. (2003). Lithium-isotope Fractionation during continental Weathering Processes. *Earth Planet. Sci. Lett.* 214 (1), 327–339. doi:10.1016/S0012-821X(03)00348-0

Resing, J. A., Sedwick, P. N., German, C. R., Jenkins, W. J., Moffett, J. W., Sohst, B. M., et al. (2015). Basin-scale Transport of Hydrothermal Dissolved Metals across the South Pacific Ocean. *Nature* 523 (7559), 200–203. doi:10.1038/nature14577

Rosner, M., Ball, L., Peucker-Ehrenbrink, B., Blusztajn, J., Bach, W., and Erzinger, J. (2007). A Simplified, Accurate and Fast Method for Lithium Isotope Analysis of Rocks and Fluids, and δ7Li Values of Seawater and Rock Reference Materials. *Geostand Geoanalyt Res.* 31 (2), 77–88. doi:10.1111/j.1751-908X.2007.00843.x

Ryan, W. B. F., Carbotte, S. M., Coplan, J. O., O'Hara, S., Melkonian, A., Arko, R., et al. (2009). Global Multi-Resolution Topography Synthesis. *Geochem. Geophys. Geosyst.* 10 (3), 1–9. doi:10.1029/2008GC002332

Ryu, J., Hong, J., Park, I.-S., Ryu, T., and Hong, H.-J. (2020). Recovery of Strontium (Sr2+) from Seawater Using a Hierarchically Structured MnO2/C/Fe3O4 Magnetic Nanocomposite. *Hydrometallurgy* 191, 105224. doi:10.1016/j.hydromet.2019.105224

Sahoo, S. K., and Masuda, A. (1998). Precise Determination of Lithium Isotopic Composition by thermal Ionization Mass Spectrometry in Natural Samples Such as Seawater. *Analytica Chim. Acta* 370 (2), 215–220. doi:10.1016/S0003-2670(98)00307-9

Sarradin, P. M., and Legrand, J. (2019). MOMARSAT2019 Cruise, RV Pourquoi Pas ? doi:10.17600/18001110 Available at: https://campagnes.flotteoceanographique.fr/campagnes/18001110/

Singerling, S. A., and Ober, J. A. (2018). *Strontium*. USGS.

Stoffynegli, P., and Mackenzie, F. T. (1984). Mass Balance of Dissolved Lithium in the Oceans. *Geochimica et Cosmochimica Acta* 48 (4), 859–872. doi:10.1016/0016-7037(84)90107-8

Teagle, D. A. H., Bickle, M. J., and Alt, J. C. (2003). Recharge Flux to Ocean-ridge Black Smoker Systems: A Geochemical Estimate from ODP Hole 504B. *Earth Planet. Sci. Lett.* 210 (1–2), 81–89. doi:10.1016/S0012-821X(03)00126-2

Tomascak, P. B., Magna, T., and Dohmen, R. (2016). *Advances in Lithium Isotope Geochemistry*. Springer International Publishing. doi:10.1007/978-3-319-01430-2

Tomascak, P. B., Tera, F., Helz, R. T., and Walker, R. J. (1999). The Absence of Lithium Isotope Fractionation during basalt Differentiation: New Measurements by Multicollector Sector ICP-MS. *Geochimica et Cosmochimica Acta* 63 (6), 907–910. doi:10.1016/S0016-7037(98)00318-4

Trezzi, G., Garcia-Orellana, J., Rodellas, V., Masqué, P., Garcia-Solsona, E., and Andersson, P. S. (2017). Assessing the Role of Submarine Groundwater Discharge as a Source of Sr to the Mediterranean Sea. *Geochimica et Cosmochimica Acta* 200, 42–54. doi:10.1016/j.gca.2016.12.005

Vance, D., Teagle, D. A. H., and Foster, G. L. (2009). Variable Quaternary Chemical Weathering Fluxes and Imbalances in marine Geochemical Budgets. *Nature* 458 (7237), 493–496. doi:10.1038/nature07828

Vigier, N., Decarreau, A., Millot, R., Carignan, J., Petit, S., and France-Lanord, C. (2008). Quantifying Li Isotope Fractionation during Smectite Formation and Implications for the Li Cycle. *Geochimica et Cosmochimica Acta* 72 (3), 780–792. doi:10.1016/j.gca.2007.11.011

Vikström, H., Davidsson, S., and Höök, M. (2013). Lithium Availability and Future Production Outlooks. *Appl. Energ.* 110, 252–266. doi:10.1016/j.apenergy.2013.04.005

Von Damm, K. L., Bray, A. M., Buttermore, L. G., and Oosting, S. E. (1998). The Geochemical Controls on Vent Fluids from the Lucky Strike Vent Field, Mid-Atlantic Ridge. *Earth Planet. Sci. Lett.* 160 (3), 521–536. doi:10.1016/S0012-821X(98)00108-3

von Strandmann, P. A. E. P., Kasemann, S. A., and Wimpenny, J. B. (2020). Lithium and Lithium Isotopes in Earth's Surface Cycles. *Elements* 16 (4), 253–258. doi:10.2138/gselements.16.4.253

Wilckens, F. K., Reeves, E. P., Bach, W., Seewald, J. S., and Kasemann, S. A. (2019). Application of B, Mg, Li, and Sr Isotopes in Acid-Sulfate Vent Fluids and Volcanic Rocks as Tracers for Fluid-Rock Interaction in Back-Arc Hydrothermal Systems. *Geochem. Geophys. Geosystems* 20, 5849–5866. doi:10.1029/2019gc008694

Conflict of Interest: The authors declare that the research was conducted in the absence of any commercial or financial relationships that could be construed as a potential conflict of interest.

Publisher's Note: All claims expressed in this article are solely those of the authors and do not necessarily represent those of their affiliated organizations, or those of the publisher, the editors and the reviewers. Any product that may be evaluated in this article, or claim that may be made by its manufacturer, is not guaranteed or endorsed by the publisher.